Advanced Physics Research

ADVANCED PHYSICS RESEARCH Open Access

www.advphysicsres.com

RESEARCH ARTICLE OPEN ACCESS

Impedance Spectroscopy of Bifurcation Oscillations in S-Type Self-Oscillatory Devices

Gonzalo Rivera-Sierra[1] | Roberto Fenollosa[1] | Jenifer Rubio-Magnieto[1] | Nripan Mathews[2] | Si En Ng[2] | Juan Bisquert[1]

[1]Instituto de Tecnología Química (ITQ), Consejo Superior de Investigaciones Científicas-Universitat Politècnica de València, València, Spain | [2]School of Materials Science and Engineering, Nanyang Technological University, Singapore, Singapore

Correspondence: Gonzalo Rivera-Sierra (grivsie@itq.upv.es) | Juan Bisquert (jbisquer@itq.upv.es)

Received: 14 March 2026 | **Revised:** 16 April 2026 | **Accepted:** 7 May 2026

Keywords: Bifurcation | Impedance Spectroscopy | Negative Differential Resistances | Oscillatory devices

ABSTRACT

Self-sustained electronic oscillators are emerging as key building blocks for physical neuromorphic computing. Among them, S-type negative differential resistance (NDR) devices offer wide material versatility and strong tunability of their internal dynamics. While nonlinear theory predicts their stability regimes and bifurcations with high accuracy, experimental access to these regimes remains limited. Here, we combine theory and experiment to characterize the stability regimes of an S-type NDR thyristor device exhibiting self-sustained oscillations. By mapping nonlinear control-theoretic concepts onto impedance spectroscopy (IS) measurements, we show that frequency-domain characterization provides direct experimental signatures of stability, bifurcations, and oscillatory regimes, despite the intrinsically nonlinear nature of the system. The measurements further reveal the interaction between autonomous and forced oscillations, as well as entrainment and phase locking phenomena. Our results establish IS as a powerful in situ probe of nonlinear dynamical behavior in oscillatory devices, with direct relevance for neuromorphic and oscillator-based hardware.

1 | Introduction

Physical computation harnesses the intrinsic dynamics of materials and electronic devices to process information directly through their nonlinear and time-dependent responses [1–4]. Rather than abstracting computation into digital logic, physical systems perform operations by exploiting properties such as phase transitions, relaxation kinetics, synchronization, or limit-cycle oscillations. Networks of nonlinear oscillators have emerged as a particularly powerful platform for this paradigm, as their collective phases and frequencies naturally encode and transform information in tasks involving optimization, pattern classification, or temporal inference [5–8].

A broad class of physical oscillators can be constructed using a two-terminal nonlinear device connected with simple passive components such as a series resistor and a capacitor [9]. Their behavior is governed by negative differential resistance (NDR), which gives rise to self-sustained oscillations when external parameters cross a critical threshold. These oscillators are typically grouped into N-type or S-type, depending on whether the NDR occurs in the current-driven or voltage-driven regime [9–12]. The transition to oscillatory behavior through this critical threshold is often sharp and corresponds to a Hopf bifurcation, where a stationary state becomes unstable and a periodic limit-cycle emerges [13, 14].

S-type oscillators include devices whose resistance exhibits a sharp switching behavior or a delayed feedback process associated with a single slow internal state variable. Examples range from oxide-based memristive devices such as VO_2 [15, 16], to electrochemical or redox systems where nonlinear autocatalytic processes induce NDR [10, 17–21]. These systems have gained renewed interest due to the role of oscillators in physical computing schemes, where the tunability of oscillation frequency, phase, and amplitude is central to exploiting coupled networks for computational tasks [22, 23].

In recent work, we summarized the dynamical properties of S-type oscillators that arise from a single resistive degree of freedom, including the approach to the Hopf bifurcation, the nature of harmonic oscillations near the onset, and the emergence of relaxation oscillations at stronger driving [5, 24].

While most studies of nonlinear oscillators focus on time-domain responses, frequency-domain analysis offers unique insight into stability, internal time constants, and the emergence of bifurcations. Impedance spectroscopy (IS), based on applying a small sinusoidal voltage or current perturbation over a range of frequencies, is widely used in electrochemical and solid-state systems to characterize dynamic processes [25–27]. In oscillatory or near-bifurcating systems, IS captures how small fluctuations evolve and dissipate, revealing signatures of NDR, eigenmode softening, and the approach to instability [12, 14, 17, 28–31]. As shown theoretically in previous work, Hopf bifurcations have a direct counterpart in the IS response of the system. Equivalent-circuit (EC) representations then allow one to track how the effective resistive and capacitive elements vary as the operating point approaches the bifurcation threshold [14]. More generally, IS can be viewed as an experimental analogue of classical control theory approaches used to analyze electronic oscillators, such as the Barkhausen or Nyquist criteria [32, 33] and the local activity theory introduced by Chua [34–36]. In these frameworks, stability and oscillatory regimes are determined by the location of the transfer function poles and zeros in the complex plane. The impedance is itself the system transfer function, experimentally accessed along the imaginary axis $s = i\omega$, where ω is the frequency, thus establishing a natural bridge between IS measurements and classical control-theoretic descriptions of oscillatory dynamics.

The general properties of S-type systems have been demonstrated with a thyristor oscillator [24] that provides a prototypical system in which these behaviors can be cleanly observed and modelled. A thyristor is a bistable PNPN device with two stable operating points: blocking and conduction [37]. Its galvanostatic current–voltage (I–V) curve exhibits three branches: a low-current blocking branch, an unstable NDR region, and a high-current conduction branch. In the potentiostatic case, at low applied voltage the device remains in the blocking state, conducting only leakage current. When the voltage reaches a threshold, a small gate current can trigger internal carrier multiplication, causing a rapid transition to the conduction branch. Once switched on, the device remains in the high-conductance state until the external current is reduced below the holding current, at which point it returns abruptly to the blocking branch. This bistability, together with the sharp transition across the unstable region, defines the S-type NDR central to its dynamics.

Coupled with a resistor–capacitor network, this bistable behavior produces self-sustained oscillations whose detailed mechanisms we have reported previously [24]. Here, we focus on the frequency-domain characterization of the same system, showing how IS captures the evolution of the EC parameters as the operating point approaches the bifurcation and enables, at the same time, the classification of different stability regimes.

In this sense, the main contribution of the present work is to build, on the basis of previous studies of Hopf bifurcations in oscillatory devices, a direct bridge between IS and Hopf bifurcation phenomena. By experimentally validating the theoretical predictions, we demonstrate that IS provides a powerful experimental route to access nonlinear dynamical regimes and complex bifurcation behavior that may sometimes remain difficult to identify from theory alone.

The structure of the paper is as follows. First, we provide a generic study of the IS behavior of an S-type oscillator across the bifurcation point, identifying the specific EC elements that govern stability and oscillation onset. A complete formulation of the expected IS response is established, validated by experimental data from the S-type thyristor device. Section 2 introduces and analyzes a generic S-type NDR model, establishing the different stability regimes and bifurcation scenarios within a nonlinear dynamical framework. In Section 3, a small-signal analysis is applied to this model to derive the corresponding IS and the associated EC representation. Section 4 extends the same theoretical approach to a specific thyristor-based S-type NDR model. In Section 5, the IS obtained experimentally from the thyristor is analyzed in both non-oscillatory and self-oscillatory regimes. Finally, Section 6 provides a comprehensive physical interpretation and discussion of the results, and Section 7 summarizes the main conclusions of this work.

2 | Dynamical Equations and Bifurcation Properties

In essence, a neuron-like oscillator can be described by a physical model containing a conduction current that depends on an internal state variable x that causes resistive switching with a NDR sector. The standard structure of an S-type NDR oscillator is shown in Figure 1a [9–11]. It consists of the nonlinear element (green), and external elements resistor R_0 and capacitor C_0, that enable an oscillatory voltage u. The I_0 is the external current and V_a the external voltage. We always have

$$I_0 = \frac{V_a - u}{R_0} \tag{1}$$

The oscillatory system is described by two dynamical equations [5].

$$\frac{du}{dt} = F = \frac{1}{C_0}\ [I_0 - g(x)u] \tag{2}$$

$$\frac{dx}{dt} = G = \frac{1}{\tau_k}\ [g(x)u - x] \tag{3}$$

Equation (2) is obtained from the addition of currents in Figure 1a,

$$I_0 = C_0\,\frac{du}{dt} + I_1 \tag{4}$$

Equation (2) describes the operation at constant current I_0, in which R_0 does not influence the bifurcation properties. The

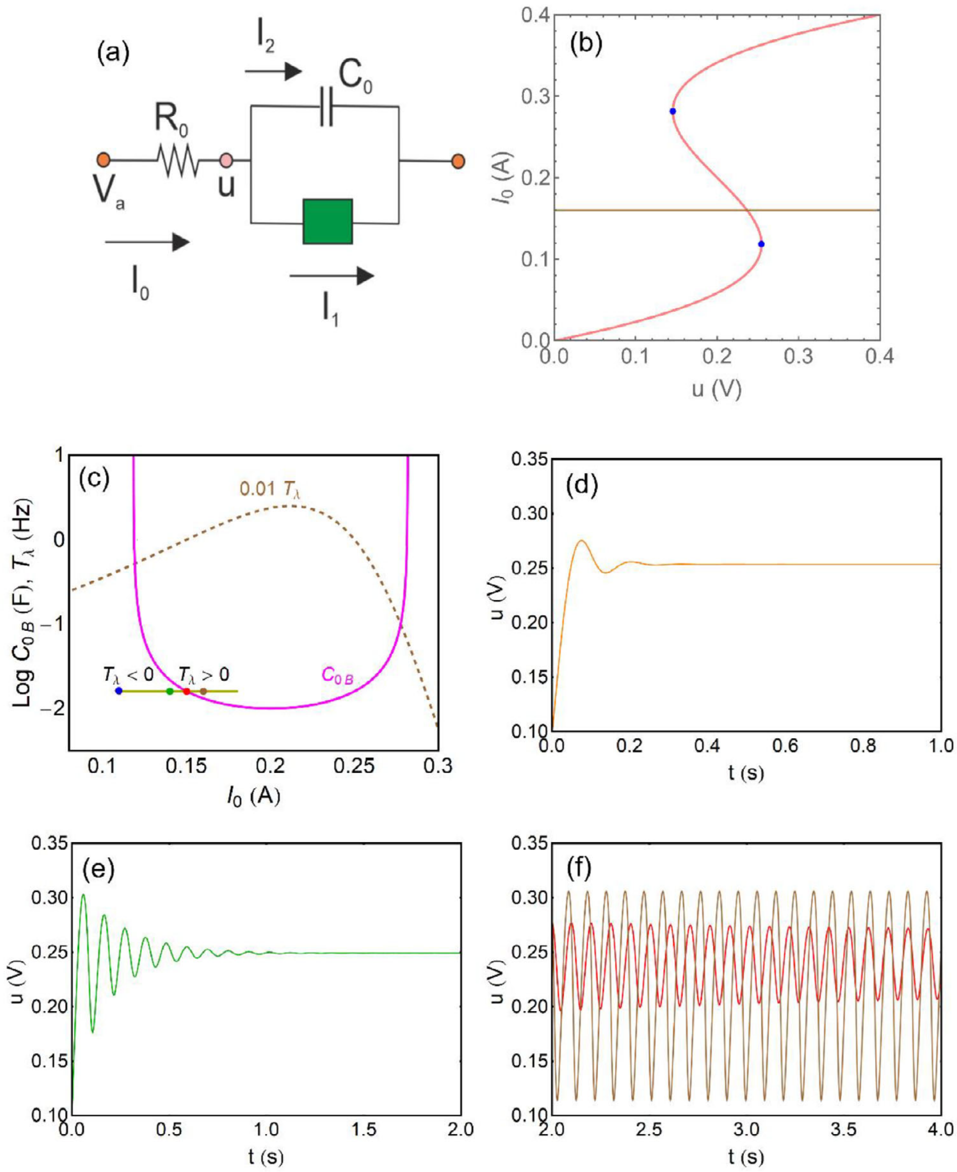

FIGURE 1 | (a) Oscillatory circuit. (b) Stationary curve $u(I_0)$ (red) and constant current line for the cubic current model $u(I_0) = a[(I_0 - b)^3 + b^3] - cI_0$. The folding points are indicated. (c) Bifurcation characteristics for constant applied current. The pink line is the value of capacitance that gives $T_\lambda = 0$ at each I_0. For $I_0 = 0.15\,A$, it is $C_{0B} = 0.016$ F (red point). The brown dashed line is T_λ for this value $C_0 = 0.016$ F, and the olive-green horizontal line indicates a change of current at fixed $C_0 = 0.016$ F ($I_0 = 0.10\,A$, $I_0 = 0.14\,A$, $I_0 = 0.15\,A$ and $I_0 = 0.16\,A$ respectively). The behavior of the potential $u(t)$ at each current is shown in (d–f). Parameters $a = 50\ V/A^3$, $b = 0.2\,A$, $c = 1\ \Omega$, $\tau_k = 0.01\ s$.

second Equation (3) states the time dependence of the internal variable x that determines the conductance g of the nonlinear element. We assume that the conductance depends on x as follows [38]

$$I_1 = g(x)\,u \tag{5}$$

The $g(x)$ is the physical function that fixes the specific model. In Equation (3) we introduce τ_k, the relaxation time for the transition of x between the two conductance branches.

An equilibrium point is given by the conditions $\dot{u} = \dot{x} = 0$. For $\dot{u} = 0$

$$u = \frac{I_0}{g(x)} \tag{6}$$

For $\dot{x} = 0$ it is

$$u = \frac{x}{g(x)} \tag{7}$$

Equation (6) gives the stationary I–V curve, as $x = I_0$ in equilibrium.

In S-type oscillators the function $u(I_0)$ is single valued. The differential resistance is

$$R_d = \frac{du}{dx} = \frac{1 - g'u}{g} \tag{8}$$

The region of NDR is when $g'u > 1$. The condition $du/dx = 0$ defines the folding points of the I–V curve. They satisfy

$$g'(x_F)\,u\,(x_F) = 1 \tag{9}$$

To illustrate a characteristic S-shape I–V curve, in the first part of the paper we use a cubic function of the type [5, 12, 39]

$$u_c(I_0) = a\left[(I_0 - b)^3 + b^3\right] - cI_0 \tag{10}$$

in terms of parameters a, b, c. Later on we use the specific form of a thyristor oscillator [24].

Equation (10) is shown in the pink curve in Figure 1b, that indicates equilibrium points when the system is measured at fixed current (as the horizontal line cases). The conductance function is

$$g\,(x) = \frac{1}{a\,(x^2 - 3bx + 3\,b^2) - c} \tag{11}$$

The turning (fold) points have the values

$$I_{F1} = b + \left(\frac{c}{3a}\right)^{1/2} \tag{12}$$

$$I_{F2} = b - \left(\frac{c}{3a}\right)^{1/2} \tag{13}$$

They are indicated in Figure 1b as blue dots.

Let us summarize the bifurcation characteristics of the circuit in Figure 1a described by the dynamical Equations (2) and (3), derived in the Appendix and explained in more details elsewhere [5, 24]. We get the Jacobian matrix

$$J = \begin{bmatrix} -\frac{g}{C_0} & -\frac{g'u}{C_0} \\ \frac{g}{\tau_k} & \frac{1}{\tau_k}(g'u - 1) \end{bmatrix} \tag{14}$$

and expressions of the trace

$$T_\lambda = -\frac{g}{C_0} + \frac{1}{\tau_k}(g'u - 1) \tag{15}$$

and the determinant

$$\Delta_\lambda = \frac{g}{C_0\tau_k} \tag{16}$$

The determinant is always positive, $\Delta_\lambda > 0$. The bifurcation diagram is shown in Figure 1c. The bifurcation region with respect to (I_0, C_0) is given by $T_\lambda = 0$, and the limit-cycle oscillations occur for $T_\lambda > 0$. The value of the capacitor at the bifurcation (pink line) is

$$C_{0B} = \tau_k\,\frac{g}{g'u - 1} \tag{17}$$

By changing the current along the green line, at fixed C_0, we pass first across the folding point I_{F2}, then across the bifurcation, and we change from stable behavior, Figure 1d,e to limit-cycle oscillations. The frequency of oscillations at the Hopf bifurcation is

$$\omega_0 = \Delta_\lambda^{1/2} = \left(\frac{g}{C_0\tau_k}\right)^{1/2} \tag{18}$$

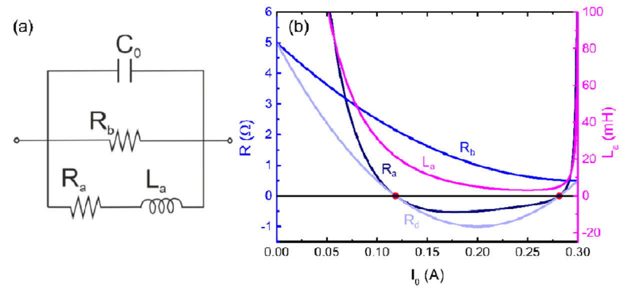

FIGURE 2 | (a) Small perturbation EC. (b) IS parameters as a function of current. Parameters $a = 50\ V/A^3$, $b = 0.2\,A$, $c = 1\,\Omega$, $\tau_K = 0.01\ s$.

This is the harmonic oscillation around the stationary point, Figure 1f (red line). If we move away from the bifurcation, the system (2, 3) produces relaxation oscillations, characterized by sudden transitions, Figure 1f (brown line) [40–42].

Strictly speaking, the full Hopf bifurcation theorem also requires the usual transversality and nondegeneracy conditions, including the speed of passage of the eigenvalues through the imaginary axis and the sign of a stability index governing the local character of the bifurcation. In the present work, we do not pursue a full mathematical proof, but adopt the standard physics and engineering approach, where these conditions are often left implicit and assumed to be satisfied, as supported here by numerical simulations and experimental evidence [43, 44].

3 | Impedance Spectroscopy Analysis

The IS measurement is the relation of voltage to current under a sinusoidal perturbation $\hat{I}$ of angular frequency ω_f. By adding the forcing term in Equations (2) and (3), the linearized Equation (14) becomes [29]

$$\frac{dX}{dt} = J\,X + \begin{pmatrix} \frac{\hat{I}}{C_0} \\ 0 \end{pmatrix} \tag{19}$$

In the frequency domain we obtain

$$\left(J - i\omega_f\,[1]\right)X = \begin{pmatrix} \frac{\hat{I}}{C_0} \\ 0 \end{pmatrix} \tag{20}$$

where [1] is the identity matrix. The impedance is defined by

$$Z = \frac{\hat{u}}{\hat{I}} = -\frac{1}{det\,(J - i\omega_f\,[1])}\frac{1}{C_0}\left(\frac{g'u - 1}{\tau_k} - i\omega_f\right) \tag{21}$$

It can be written in several equivalent ways

$$Z = \frac{1}{C_0}\frac{1}{(\omega_0 - \omega_f)(\omega_0 + \omega_f) + i\omega_f T_\lambda}\left(\frac{g}{C_0} + T_\lambda - i\omega_f\right) \tag{22}$$

$$Z = \left[g + i\,\omega_f C_0 + \frac{(gg'u)}{(1 - g'u) + i\,\omega_f\tau_k}\right]^{-1} \tag{23}$$

On another hand, the impedance can be expressed in terms of the EC shown in Figure 2a [14]

$$Z = \left[\frac{1}{R_b} + i\,\omega_f C_0 + \frac{1}{(R_a + i\omega_f L_a)} \right]^{-1} \tag{24}$$

Comparing Equations (23) and (24), the small perturbation EC elements are

$$R_b = \frac{1}{g} \tag{25}$$

$$R_a = \frac{1 - g'u}{g\,g'u} \tag{26}$$

$$L_a = \frac{\tau_k}{g\,g'u} \tag{27}$$

The variation of these elements with the stationary applied current is shown in Figure 2b. R_b and L_a remain positive, while R_a is negative between the folding points, producing a total differential resistance R_d

$$R_d = \left[\frac{1}{R_b} + \frac{1}{R_a} \right]^{-1} \tag{28}$$

We remark that the determinant remains positive even though the total differential resistance is negative [30].

We now examine the characteristic time scales associated with the key elements of the EC and relate them to the intrinsic response times of the NDR device, the external capacitor, and the overall circuit dynamics, as well as to the emergence of stable, unstable, and bifurcation regimes. The characteristic time of the inductive branch of the EC is given by

$$\tau_L = \frac{L_a}{R_a} = \frac{\tau_k}{1 - g'u} \tag{29}$$

while the characteristic charging time of the capacitive branch is

$$\tau_C = R_b\ C_0 = \frac{C_0}{g} \tag{30}$$

and the intrinsic relaxation time of the S-type device is given by

$$\tau_k = \frac{L_a}{R_a + R_b} \tag{31}$$

which reflects the internal dynamics of the S-type active element embedded in the circuit.

Since L_a is always positive whereas R_a changes sign across the NDR region, the inductive time τ_L becomes negative within the NDR regime. However, this quantity alone does not provide a direct criterion for the stability of the full system, as it is obtained by separating individual circuit elements and does not account for the feedback loop formed by the complete resonant network. To assess the stability of the linearized dynamics, it is necessary to introduce an effective characteristic time of the EC that governs the relaxation (or amplification) of small perturbations around the operating point. This effective relaxation time corresponds to the linearized RLC feedback loop and is given by the parallel combination of the capacitive and inductive time scales,

$$\frac{1}{\tau_{eq}} = \frac{1}{\tau_C} + \frac{1}{\tau_L} \tag{32}$$

This effective time scale is directly related to the trace of the Jacobian matrix of the dynamical system,

$$T_\lambda = -\frac{1}{\tau_{eq}} \tag{33}$$

Consequently, τ_{eq} provides a compact dynamical criterion for stability: when $\tau_{eq} > 0$, small perturbations are damped and the stationary state is stable; when $\tau_{eq} < 0$, perturbations are amplified, leading to self-sustained oscillations; and the marginal condition $\tau_{eq}^{-1} = 0$ marks the onset of the Hopf bifurcation separating stable and oscillatory regimes.

In addition, the characteristic times introduced above are linked to the determinant of the Jacobian and therefore to the oscillation frequency at the bifurcation point. In particular, the Hopf frequency is determined by the coupling between the intrinsic relaxation time of the active S-type device, τ_K, and the capacitive time of the passive branch, τ_C,

$$\omega_0 = \Delta_\lambda^{1/2} = \left(\frac{1}{\tau_K \tau_C} \right)^{1/2} \tag{34}$$

highlighting that the oscillatory dynamics emerge from the interplay between the internal device kinetics (thyristor) and the external circuit response (external capacitor coupled).

The relationship between the effective circuit time scales and the trace-determinant structure of the Jacobian has been derived previously within a general theoretical review in Ref. [14]. The present expressions represent a direct implementation of that formalism for the S-type NDR system analyzed here, providing an explicit mapping between EC parameters and the onset of instability.

Now we follow the spectral changes of IS as we move the stationary current along the I–V curve, as indicated in Figure 3a. The corresponding changes of DC resistance are shown in Figure 3b, showing clearly the region of negative resistance.

Starting from the lowest current values, the system exhibits a purely capacitive response in Figure 3c, which evolves into a chemical inductor impedance [30, 45] in Figure 3d, characterized by the characteristic crossing into the fourth quadrant, as discussed previously [14]. The visibility of the inductive feature depends on the relative magnitudes of the capacitive and inductive branches elements. Upon approaching the lower folding point, the effective inductance increases markedly and the DC resistance vanishes, leading to a circular impedance response, as shown in Figure 3e. Beyond this point, the DC resistance becomes negative. When the Hopf bifurcation is crossed and the system enters the unstable regime, the impedance spectra undergo a mirror inversion from the right half-plane to the left half-plane, yielding responses that are qualitatively analogous to those observed in the stable regime but reflected across the imaginary axis, as illustrated in Figure 3f,g. Upon further increasing the current, a second inversion of the spectra is observed when the system crosses back through the bifurcation boundary, returning the imaginary space response to the right half-plane even though the DC resistance remains negative, Figure 3h. Finally, upon approaching and crossing the upper

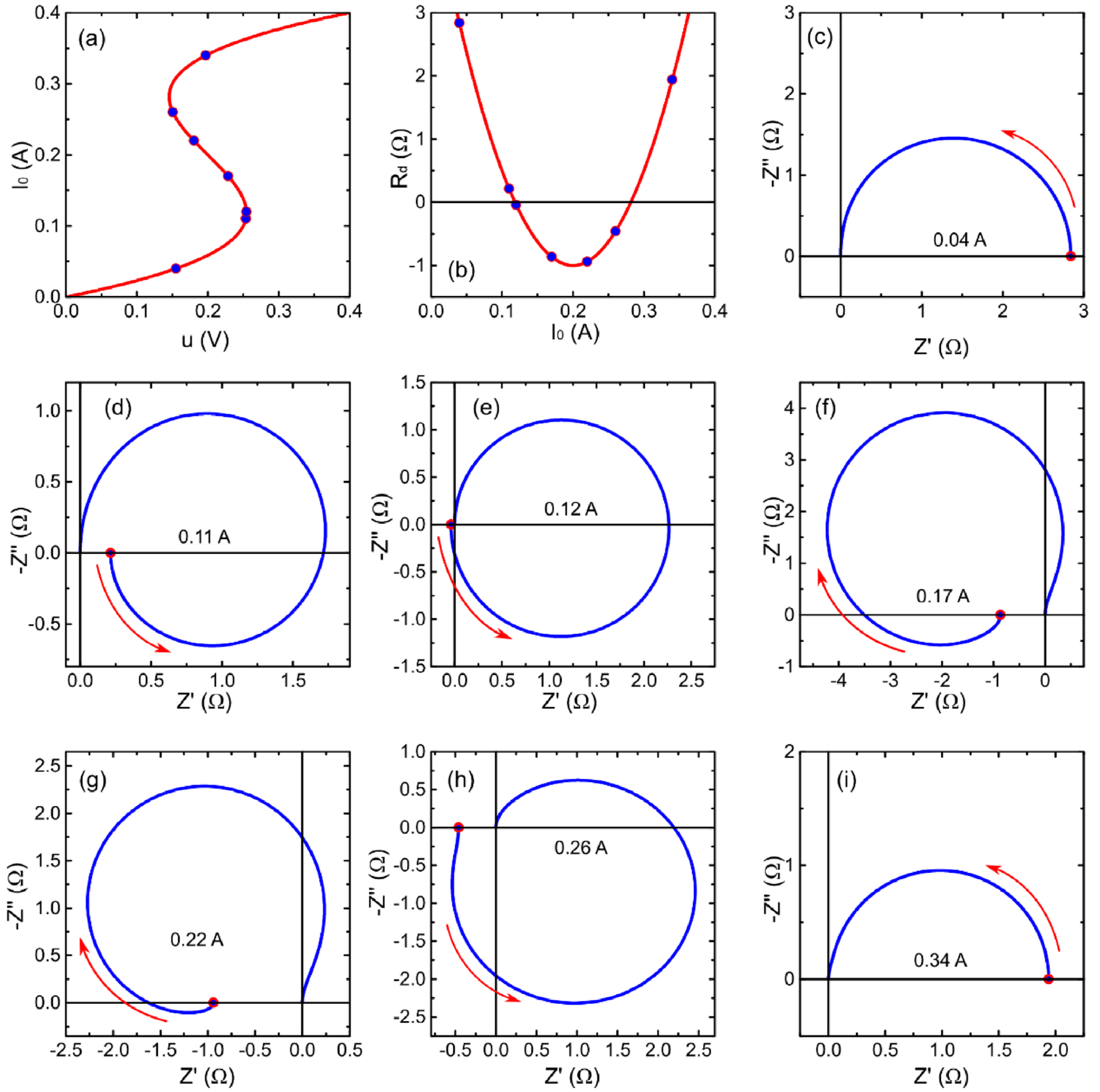

FIGURE 3 | (a) I–V curve and (b) DC resistance of the S-model. (c–i) Impedance spectra at fixed current I_0 for the points indicated in (a). The point is the impedance at zero frequency, $R_d = Z(\omega_f = 0)$. Arrows indicate the direction of increasing frequency. Parameters $a = 50\ V/A^3$, $b = 0.2\ A$, $c = 1\ \Omega$, $\tau_k = 0.01\ s$, $C_0 = 0.016$ F.

folding point, the spectra recover the initial capacitive-like response associated with positive DC resistance, as shown in Figure 3i.

We next discuss in detail in Figure 4 the evolution of the IS across the Hopf bifurcation, analyzing four points of stationary current in different colors along the green line indicated in Figure 1c, corresponding to the capacitor value 0.016 F. The NDR is onset at the current 0.118 A, and the Hopf bifurcation indicated in a red point is at the current 0.15 A. We begin with the blue point of Figure 1c at 0.11 A that gives the blue spectrum in Figure 4. This stationary point is outside of the region of NDR, hence the DC resistance R_d is positive. The spectrum shows again the characteristic shape of the chemical inductor.

The impedance spectra, evaluated at the other three points indicated in Figure 1c (green, red, brown), are shown in Figure 4. In these three points the stationary R_d value of the resistance is negative. In the green point, the system is still damped to equilibrium, while in the red point the system becomes oscillatory. The crucial property is the value of the resistance at intermediate frequencies, which switches from positive to negative across the bifurcation [28]. This is why the spectra in Figure 4a switch between the second and the fourth quadrant when the current

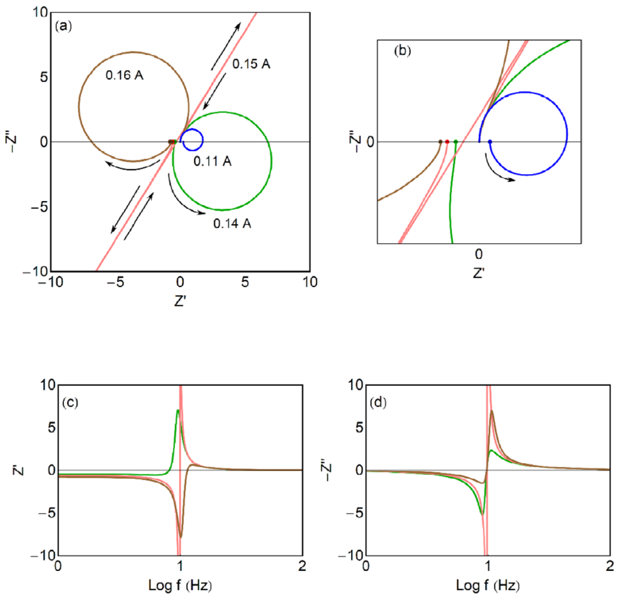

FIGURE 4 | Impedance spectra at three fixed currents for $C_0 = 0.016$ F. The oscillation frequency at the bifurcation is $\omega_{0B} = 62.0\ rad/s$, $f_{0B} = 9.87\ Hz$. Impedances in Ω. (b) is an enlargement of (a) close to the origin. The points are the impedance at zero frequency in each case. Arrows indicate the direction of increasing frequency. (c,d) Real and imaginary part of the impedance as a function of frequency. Parameters $a = 50\ V/A^3$, $b = 0.2\ A$, $c = 1\ \Omega$, $\tau_k = 0.01\ s$.

passes through the bifurcation. We note that inversion of the sign of Z' and $-Z''$ occurs when the frequency is scanned through the intrinsic oscillatory value ω_0 of Equation (18). This can be observed in the *Z vs. Log f* plots of Figure 4c,d, where $f = \omega_f/2\pi$ is the frequency. There is a singularity when the current is at the bifurcation value. The impedance starts growing toward $(-\infty, -\infty)$ at low frequency and returns from $(+\infty, +\infty)$ at high frequency. This can be rationalized observing that the denominator term in Equation (21), that becomes $det\,(J - i\omega_f[1]) = 0$, matches the eigenvalues of Equation (42) (see Appendix). In Equation (22) it is observed that the singularity occurs when $T_\lambda = 0$ at the specific frequency $\omega_f = \omega_0$. In general, the bifurcation at constant current corresponds to the poles of the impedance function [28, 29].

All the phenomena discussed here are directly connected to classical control-theoretic criteria for oscillators based on the analysis of the system transfer function, such as Chua's local activity framework or the Barkhausen and Nyquist stability criteria [34–36]. Now, the relevant transfer function is the impedance of the device-circuit system $Z(a + ib)$. Within these classical frameworks, a dynamical regime is locally stable when the poles of the transfer function lie in the left half of the complex plane, whereas instability arises when poles cross into the right half-plane. Consequently, the transition from stable to unstable operation at a Hopf bifurcation necessarily involves the crossing of a pole through the imaginary axis, that separates both half-planes. This imaginary axis is precisely the domain probed experimentally in IS, where the transfer function is evaluated along $a = 0$ and $b = \omega$ by sweeping the frequency ω. As a result, when the system is tuned to the bifurcation point or sufficiently close to it, the impedance diverges at the Hopf frequency ω. This establishes a direct and physically grounded connection between experimental IS and classical control theory for the stability of nonlinear oscillatory systems.

For a more exhaustive analysis of the evolution of the IS upon sweeping I_0, as well as of the parameters extracted from the EC representation, the reader is referred to the Section S1, with white backgrounds corresponding to the stable regime and green backgrounds indicating the unstable regime.

The present analysis applies to the small-signal response around stationary operating points. Once IS is performed within the self-oscillatory regime, the system formally becomes a periodically forced nonlinear oscillator, whose rigorous treatment would require Floquet theory or an associated Poincaré return map [43, 44].

4 | Thyristor Model

The previous sections established the general properties of IS behavior of S-type systems with a bifurcation behavior. Now we measure these characteristics on the thyristor oscillator that has been previously discussed [24]. To describe the *I–V* curve in this system, we use the analytical model

$$u_d\ (x) = R_v\ x + V_0 ln\left(\frac{d_0^2 a_0 + d_0 a_1 x + a_2 x^2}{d_0 b_0 + b_1 x + b_2 x^2}\right) + V_1 \tag{35}$$

We introduce the function

$$g\ (x) = \frac{x}{u_d\,(x)} \tag{36}$$

and define the oscillator by Equations (2) and (3).

Figure 5 presents the simulated response of the thyristor oscillator model. The *I–V* characteristic is shown in Figure 5a, where the stationary branch obtained in the absence of oscillations (for capacitance values in the stable regime) is shown in blue, while the oscillatory response (for capacitance values in the unstable oscillatory regime) is superimposed in magenta. The bifurcation diagram is displayed in Figure 5b, and simulations of oscillatory dynamics are presented in Figure 5c–f. In Figure 5c,d, oscillations obtained with a smaller external capacitance, close to the Hopf bifurcation, exhibit smaller amplitudes, higher frequencies, and a more sinusoidal character. In contrast, Figure 5e,f corresponds to a larger capacitance, further away from the bifurcation threshold, resulting in oscillations with larger amplitudes, lower frequencies, and a relaxation-type waveform. All these predictions have been experimentally observed in Ref. [24].

The simulated IS of the thyristor model is obtained following exactly the same procedure as that employed in the previous sections for the general S-type model in Equations (19–24). The resulting spectra exhibit the same qualitative features across the different dynamical regimes, namely stable, bifurcation, and unstable (oscillatory) operation. Simulated IS for different values of I_0 and the corresponding EC parameters are shown in the Section S2.1, with white backgrounds corresponding to the stable regime and green backgrounds indicating the unstable regime.

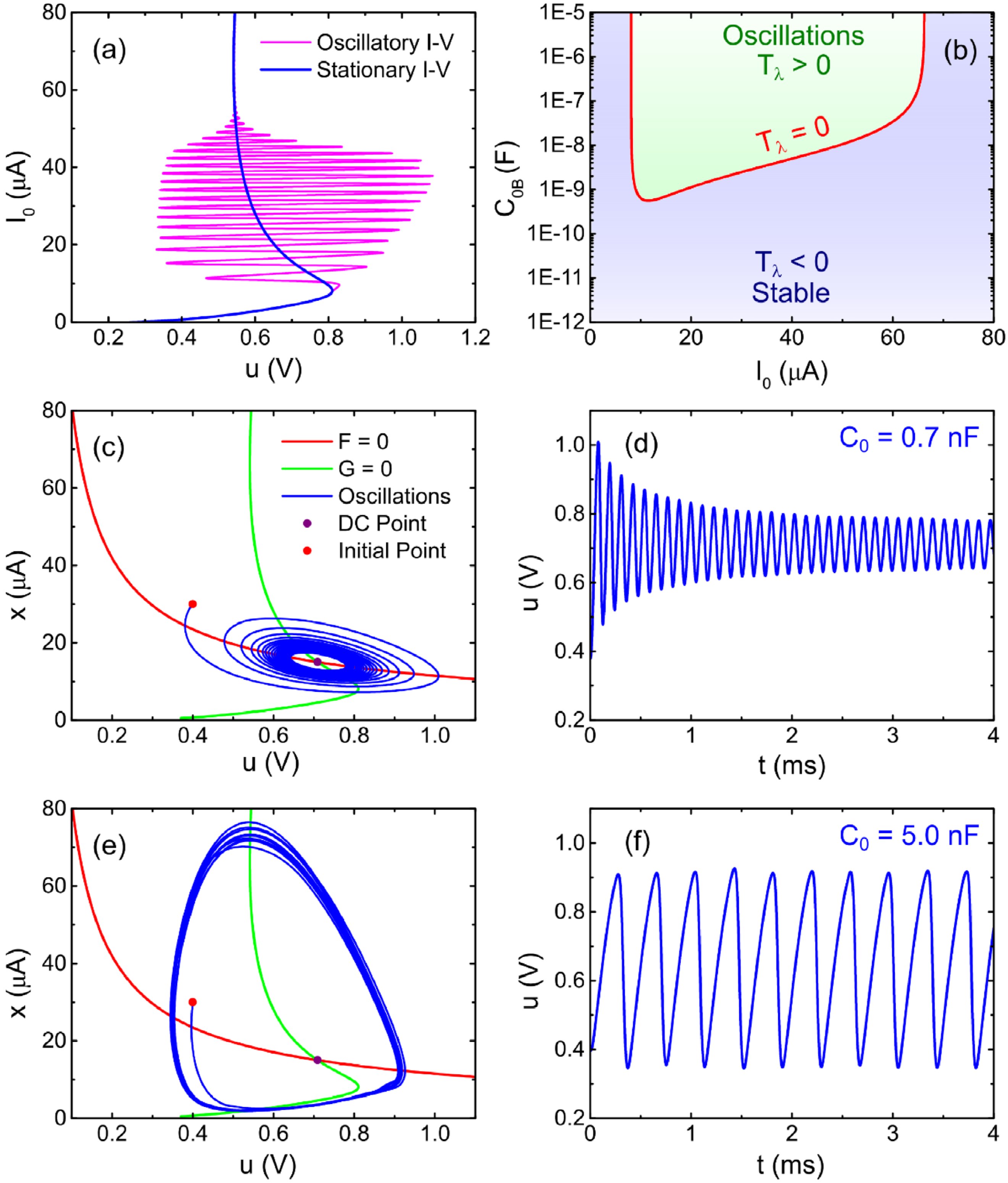

FIGURE 5 | Simulated thyristor dynamics. (a) Stationary *I–V* curve (blue) and oscillatory response obtained with an external capacitor $C_0 = 5.0\ nF$ under a triangular current sweep (rate 1 mA/s), shown in pink. (b) Bifurcation diagram as a function of the external capacitance and imposed current, identifying stable, oscillatory, and bifurcation regimes. (c–f) Phase-space trajectories and time-domain voltage oscillations for $I_0 = 15\ \mu A$ with $C_0 = 0.7\ nF$ (c,d) and $C_0 = 5.0\ nF$ (e,f). Parameters $R_v = 0.0023\ M\Omega$; $V_0 = 0.124\ V$, $V_1 = 0.740\ V$; $d_0 = 1.864$; $a_0 = 0.0538$; $a_1 = 0.238\ \mu A^{-1}$; $a_2 = -3.061\ 10^{-7}\ \mu A^{-2}$; $b_0 = 4.872$; $b_1 = -1.964\ \mu A^{-1}$; $b_2 = 0.142\ \mu A^{-2}$; $\tau_K = 20\ \mu s$.

5 | Experimental Results: Thyristor IS and Oscillations

Next, we analyze the features observed in the experimental IS and relate them to the dynamical regimes of the device. Impedance spectra are measured at selected current points along the *I–V* characteristic under two different conditions. In Figure 6, the thyristor is characterized without an external capacitor, so that the only capacitance present is the intrinsic parasitic capacitance of the device. In this case, the effective capacitance is small and the system remains below the Hopf bifurcation threshold, such that no intrinsic oscillations are observed. In contrast, in Figure 7 an external capacitor of 4.5 nF is added and the system exhibits clear self-sustained oscillations, as shown in Figure 5f. Under these oscillatory conditions, the intrinsic limit-cycle dynamics can interact and mix with the small-amplitude sinusoidal perturbation imposed during the IS. Therefore, a proper interpretation of the experimental IS response becomes crucial to correctly perform in situ nonlinear analysis and to avoid misinterpreting dynamical effects as purely linear circuit features.

These figures illustrate how the IS evolves with the applied current. In the non-oscillatory case (Figure 6), it is worth noting that the DC resistance changes from positive to negative and back to positive, as expected from the *I–V* characteristic, without any inversion of the response into the left half-plane. This is because the small parasitic capacitance of the device prevents the system from crossing the Hopf bifurcation threshold and entering an unstable oscillatory regime.

When analyzing the IS of the thyristor in the oscillatory case (Figure 7), the initial and final spectra (red, orange, and dark green traces) follow the qualitative response expected from the capacitive arc and the chemical inductor, with a pronounced increase in the impedance magnitude as the bifurcation point is approached (orange trace), consistent with the divergence expected at the Hopf bifurcation. However, within the unstable regime, the measured spectra do not invert into the left half-plane as predicted by the theory (see Figure 4). Instead, they exhibit a marked increase in spectral noise. In addition to these features, in both thyristor conditions, the measurements display a discrete switching between two values of the real part of the impedance at very low frequency, corresponding to alternating positive and negative values of Z' when $Z'' = 0$.

These experimental spectra were fitted using the EC introduced in Figure 2a, and the extracted EC parameters are reported in Figure 8 for the non-oscillatory case and in Figure 9 for a direct comparison between non-oscillatory and oscillatory cases. These results show that, except for the externally imposed capacitance, the extracted parameters are essentially independent of whether the device is oscillating or not, their magnitudes and trends remain unchanged across both conditions. As expected, we see in Figure 9b that the only parameter that differs between the two operating modes is the effective capacitance C_0, which exhibits the remarkable behavior of collapsing from the externally imposed value $C_0 \approx 4.5\,nF$ to the intrinsic parasitic capacitance of the device $C_0 \approx 0.1\,nF$ when the current lies within the oscillatory regime. This is a key indication that IS does not actually detect the presence of the external capacitor during the oscillations. Finally, the intrinsic relaxation time of the thyristor τ_K remains approximately constant, as evidenced in Figures 8e and 9d, in agreement with theoretical expectations. The slight decrease observed at high currents can be attributed to an artificial increase in the fitted capacitance at high current values, Figure 8c, likely reflecting additional high-current capacitive contributions not included in the model, which do not affect the main physical interpretation.

6 | Interpretation and Discussion

In order to understand the origin of the observed phenomena, and especially the reason why the IS does not switch to the second and third quadrants when the system crosses the Hopf bifurcation, it is essential to recognize that the system is already oscillating when the IS is performed in this regime. In IS measurements, a small-amplitude sinusoidal perturbation is superimposed on a DC bias (galvanostatic excitation in our case), and the impedance is extracted from the phase shift between the input and output AC components together with the ratio of their amplitudes and DC levels. However, in the oscillatory regime of the device, the output signal already exhibits self-sustained oscillations with a characteristic amplitude and frequency even in the absence of any external AC perturbation. When the small AC excitation is applied under these conditions, the measured output response corresponds to the superposition of the AC-driven response onto the pre-existing autonomous oscillation of the device at the given DC operating point.

Once IS is applied within the self-oscillatory regime, the system should, strictly speaking, be understood as a periodically forced nonlinear oscillator. In this case, the rigorous mathematical framework is no longer restricted to linear stability around a stationary operating point, but instead concerns the stability, coexistence, and interaction of periodic orbits, as described by Floquet theory or the associated Poincaré return map [43, 44].

To illustrate and clarify this mechanism conceptually, raw IS time-domain signals have been simulated in Figure 10 using the general S-type model of Figure 1 in the oscillatory regime by adding a series resistance $R_0 = 1\ \Omega$ in order to amplify the AC output signal and clarify the observed phenomenon. Figure 10a displays the input current signals, all applied at the same DC bias level ($I_0 = 0.20\ mA$) but vertically offset for visual clarity and at different excitation frequencies, while Figure 10b shows the corresponding output voltage responses, again vertically offset for clarity. For a more detailed understanding of how the raw impedance signals are generated and analyzed in both the oscillatory and non-oscillatory regimes in the experimental setups, the reader is referred to Section S2.2.

As a consequence, IS effectively operates on the AC components of the input and output signals superimposed on the intrinsic oscillation of the device, and the DC output voltage entering the impedance evaluation corresponds to a time-averaged value over the temporal window used for the measurement. This immediately leads to a first key conclusion: since the external capacitance C_0 is already being periodically charged and discharged by the intrinsic oscillations in the unstable regime, it does not impose any additional phase lag on the small AC perturbation applied during IS. As a result, the experimental IS is unable to detect C_0

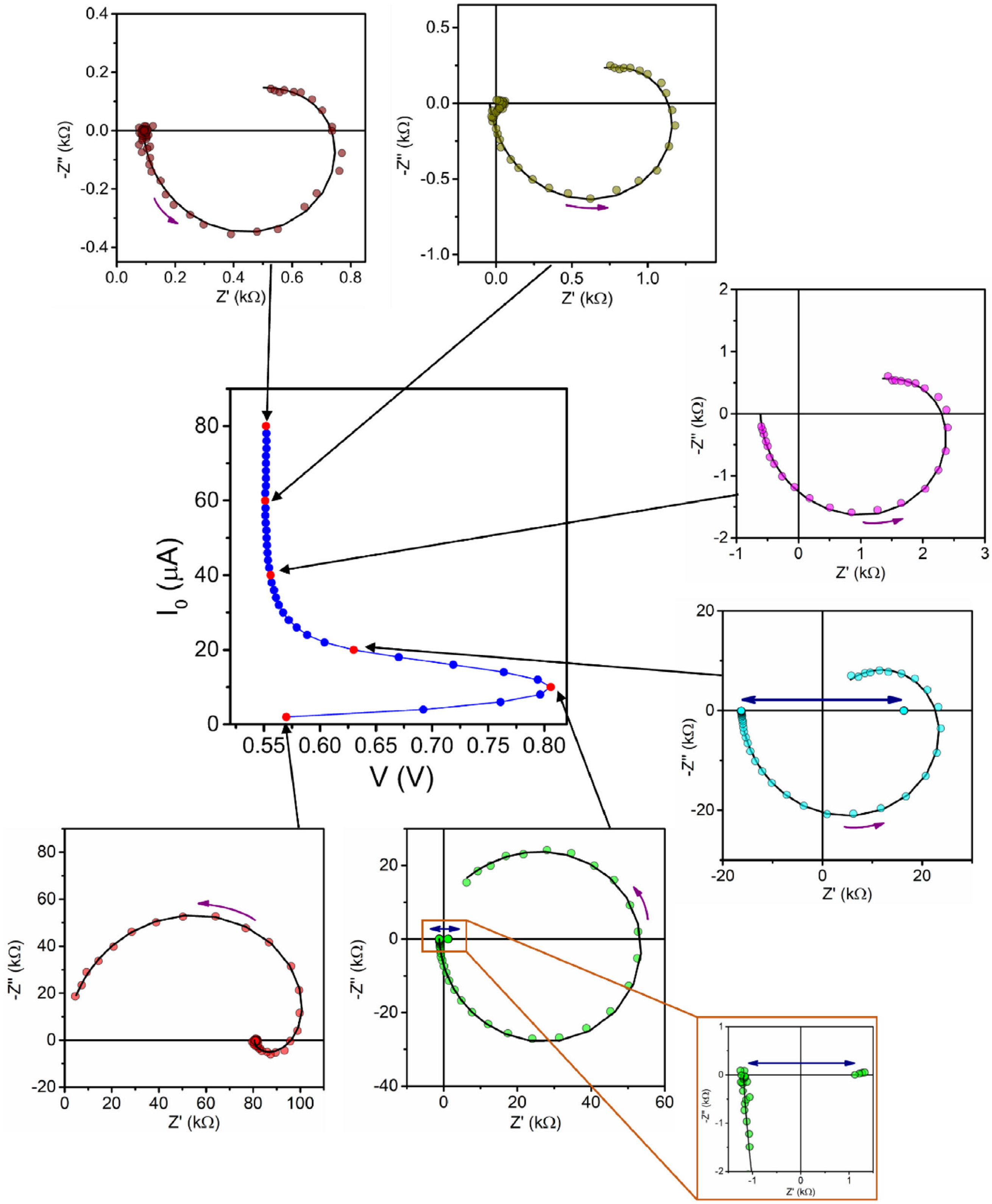

FIGURE 6 | *I–V* curve and IS evolution of the thyristor device in the absence of spiking. The central panel shows the characteristic *I–V* curve without oscillatory behavior. Insets show the corresponding impedance spectra at selected bias points. Points are the experimental data, and straight lines are the fitting results to the EC circuit of Figure 2a. Arrows indicate the direction of increasing frequency.

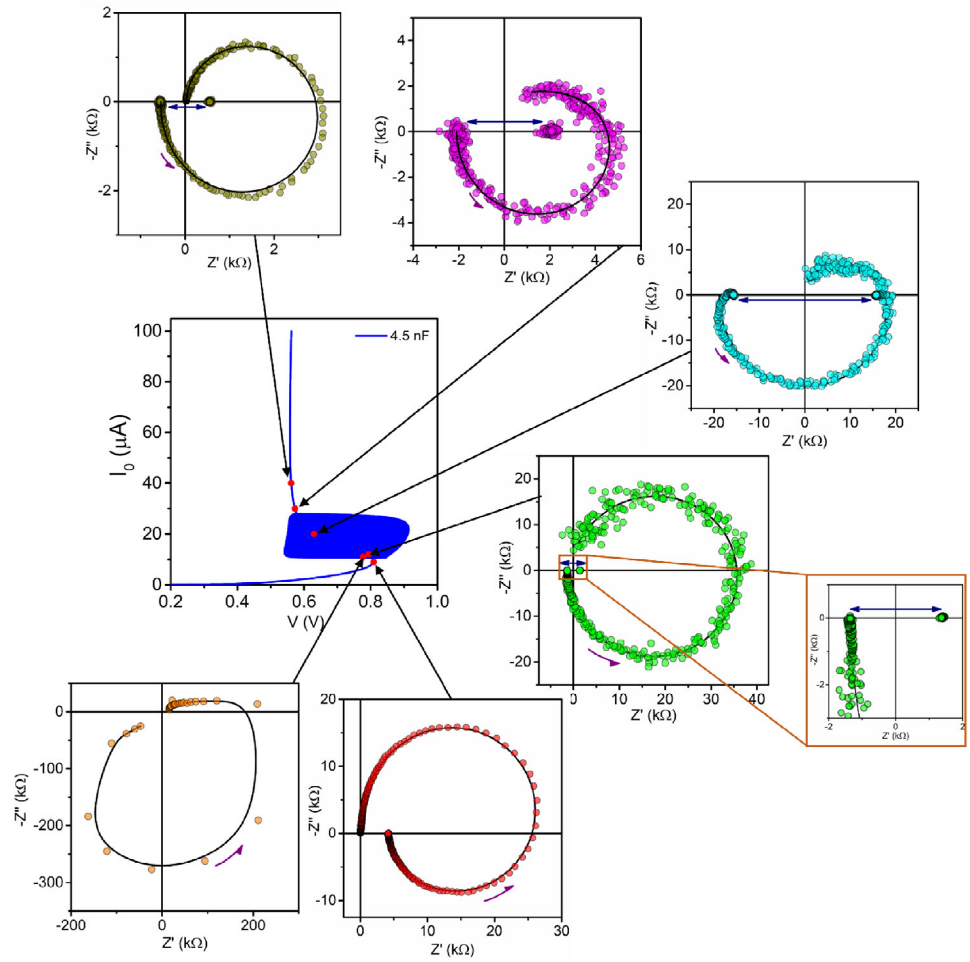

FIGURE 7 | *I–V* curve and IS evolution of the thyristor device under spiking conditions. The central panel shows the characteristic *I–V* curve with oscillatory behavior. Insets show the corresponding impedance spectra at selected bias points. Points are the experimental data, and straight lines are the fitting results to the EC circuit of Figure 2a. Arrows indicate the direction of increasing frequency.

when the device operates in the oscillatory regime. This directly explains the pronounced collapse of the fitted C_0 within the oscillatory regime and its recovery to the externally imposed value upon exiting this regime. In practice, the capacitance extracted in the oscillatory regime corresponds to the intrinsic parasitic capacitance of the device, which does not participate in the self-sustained oscillatory dynamics.

This also implies that, in the oscillatory regime, the measured AC output response effectively corresponds to that of the system without the oscillation-enabling external capacitance. Consequently, the spectra do not invert into the left half-plane, even though the DC resistance remains negative, because the effective small-signal response is that of a configuration that would not sustain oscillations.

The same reasoning directly accounts for the noise observed in the IS within the unstable regime. Depending on the excitation frequency and on the specific temporal window over which the AC components are evaluated, the IS procedure samples different portions of the intrinsic oscillation trajectory. At high excitation frequencies, the AC perturbation probes only short segments of the limit cycle, leading to strong spectral point-to-point variability and enhanced apparent noise in the extracted impedance. In contrast, at lower excitation frequencies the AC excitation spans a larger fraction of the intrinsic oscillation period, so that the signal averaging becomes more effective and the apparent noise level is substantially reduced. This frequency-dependent noise therefore constitutes a direct signature of the presence of intrinsic oscillations and of their characteristic amplitude and frequency.

Taken together, these considerations imply that the IS response of the system in the oscillatory regime reflects a mixture of the responses characteristic of stable and oscillatory operation. When the system is biased at current values for which no intrinsic oscillations occur, the impedance corresponds to the genuine small-signal response of the device-circuit system. In contrast, when the system operates within the oscillatory regime, the measured spectra correspond to the response of the same system effectively deprived of the oscillation-enabling external capacitance, with an additional noise contribution arising from the intrinsic limit-cycle dynamics.

For comparison, IS and EC parameters of the thyristor model obtained using a capacitance value that does not induce an unstable regime or bifurcations $C_0 = 0.2\ nF$, for different applied currents, are reported in the Section S2.3.

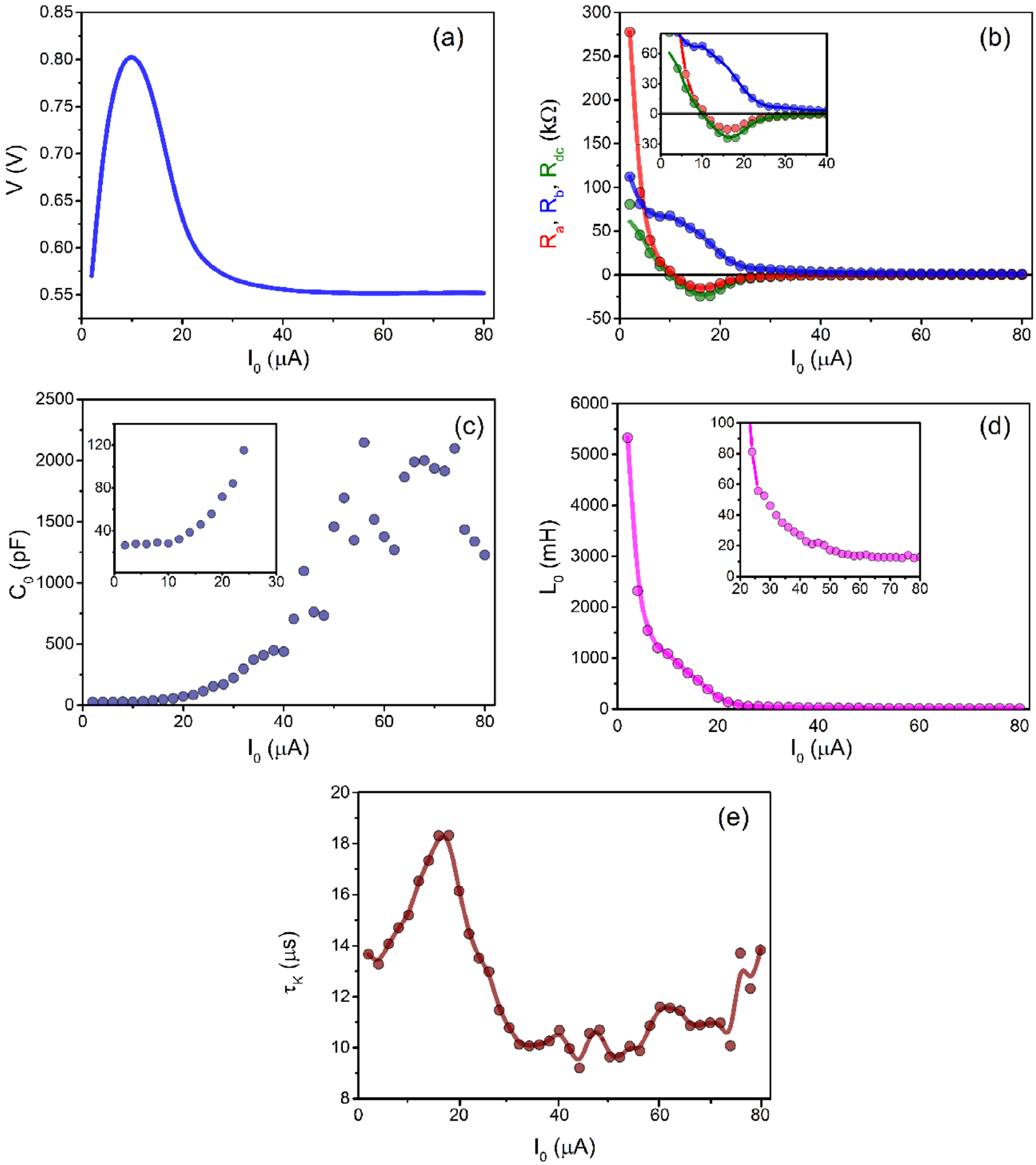

FIGURE 8 | IS experimental data and analysis for the case without oscillations. (a) I–V curve. Extracted parameters: (b) Resistances R_a, R_b and R_{dc}, (c) Capacitance C_0, (d) Inductance L_a, and (e) Characteristic response time of the thyristor τ_K. The points represent the fitted experimental data, while the lines are only guides to the eye.

Based on these results, Figure 11 presents a composite simulated replication of the experimentally observed response at current values comparable to those in Figures 6 and 7, using the oscillation-enabling capacitance outside the oscillatory region $C_0 = 4.5\ nF$ (white backgrounds) and the non-oscillatory capacitance within the oscillatory region $C_0 = 0.2\ nF$ (green backgrounds).

Accordingly, a direct comparison between the experimental IS in Figure 7 and the simulated IS in Figure 11 reveals an almost one-to-one correspondence, confirming that the behavior discussed above indeed emerges from the interaction between intrinsic device self-oscillations and the small-signal perturbation imposed during the IS measurement. Going one step further, the IS measured in the oscillatory regime in Figure 7 (green, cyan,

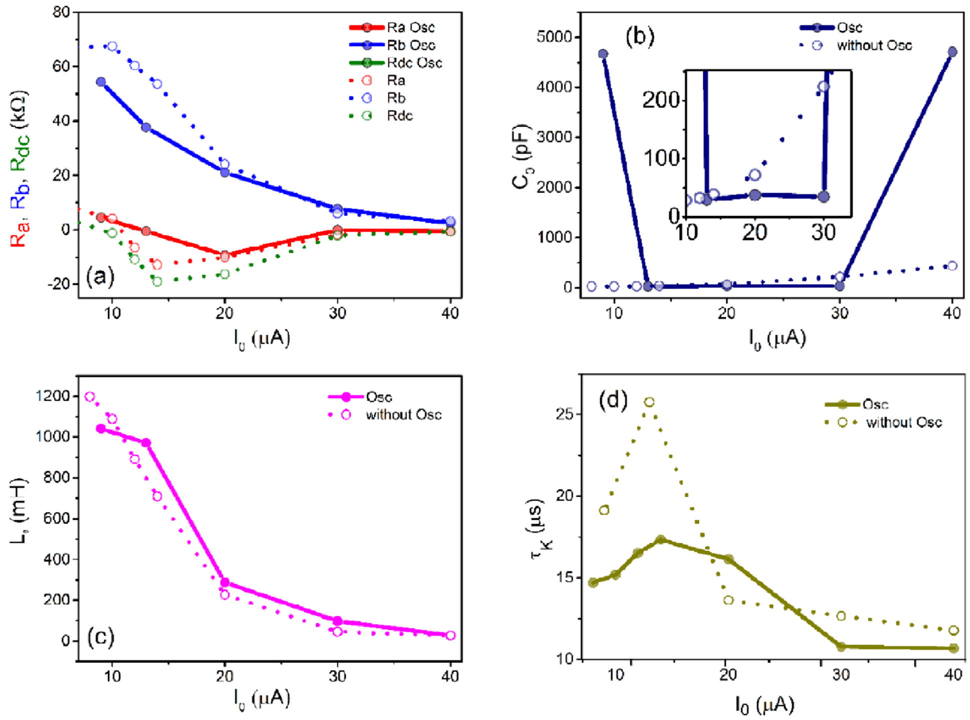

FIGURE 9 | IS experimental data and analysis with and without oscillations. Extracted parameters: (a) Resistances R_a, R_b and R_{dc}; (b) Capacitance C_0; (c) Inductance L_a; (d) Characteristic response time of the thyristor τ_K. Solid lines correspond to the case with oscillations, and dashed lines to the case without oscillations. The points represent the fitted experimental data, while the lines are only guides to the eye.

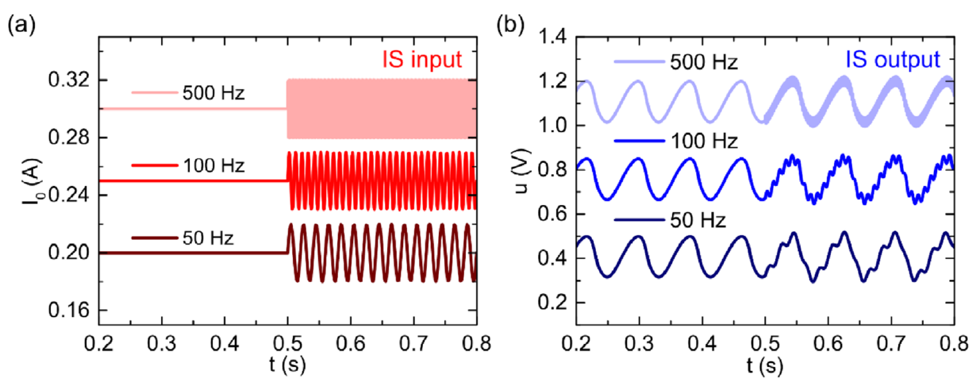

FIGURE 10 | Simulated response of a generic S-type oscillator in the unstable regime to the input signal used in IS measurements at three different excitation frequencies ($f = 50, 100, 500$ Hz). (a) Input current signals, vertically offset for clarity (cumulative offset 0.05 A). (b) Output voltage responses, vertically offset for clarity (cumulative offset 0.35 V). The simulations use the S-type model shown in Figures 1 and 3 with identical parameters.

and magenta traces) are, apart from the superimposed noise, essentially identical to the spectra obtained at the same current values in Figure 6, where the external capacitance enabling oscillations is absent. This further supports the conclusion that, within the oscillatory regime, the IS measurements effectively probe the small-signal response of the system in the absence of the oscillation-enabling capacitance, in full agreement with the superposition mechanism illustrated in Figure 10.

To enable a direct comparison between experimentally extracted parameters and model predictions, Figure 12 presents the EC parameters that remain essentially unchanged upon varying the external capacitance and, therefore, across different stability regimes. The close agreement between the simulated trends and magnitudes and those obtained experimentally in Figures 8 and 9 demonstrates the internal consistency of the model and supports the robustness of the EC representation across both oscillatory and non-oscillatory operating conditions.

To conclude this work, we address the remaining feature of the IS measurements that requires interpretation. In both sets of thyristor IS, namely those obtained with only the parasitic capacitance (Figure 6) and those obtained with the oscillation-enabling external capacitance (Figure 7), a distinctive behavior is observed at low frequencies. When the imaginary part vanishes ($Z'' = 0$) and the real part is negative ($Z' < 0$), the measured

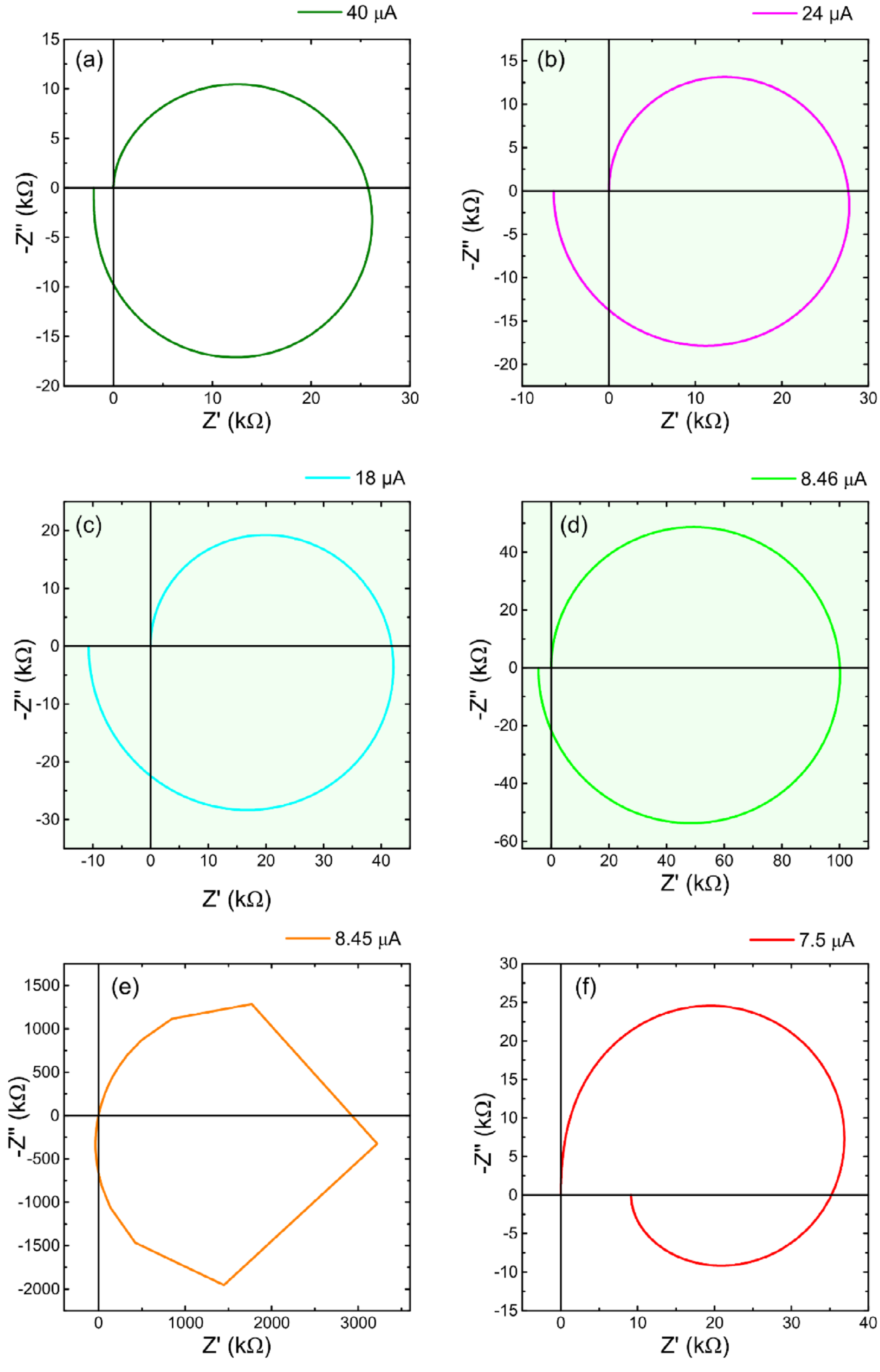

FIGURE 11 | Simulated replication of the evolution of the thyristor IS (Figure 7) using a combined modeling framework. White background spectra are using the model shown in Figure 5 for $C_0 = 4.5\ nF$ and green background spectra are using $C_0 = 0.2\ nF$, with similar current values to those used experimentally in Figures 6 and 7. Simulation model parameters are the same as in Figure 5.

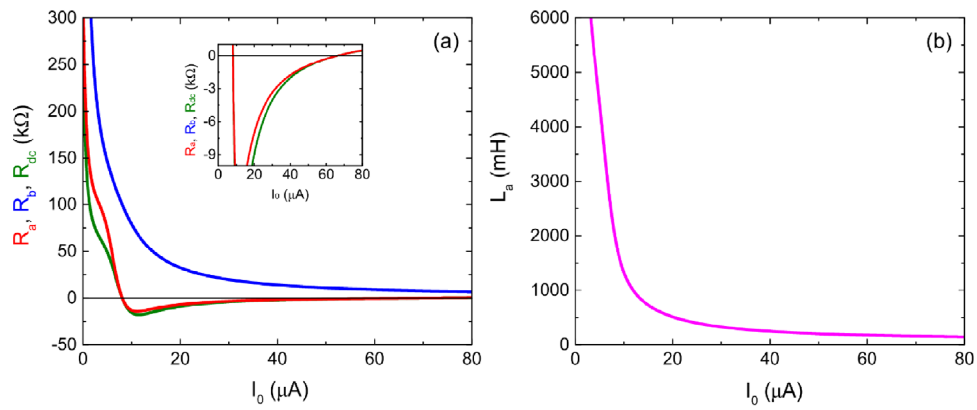

FIGURE 12 | Simulated evolution of the IS EC parameters of the thyristor model as a function of the applied current I_0. (a) Resistances R_a, R_b, and total DC equivalent resistance R_{dc}. (b) Inductance L_a. Simulation model parameters are the same as in Figure 5.

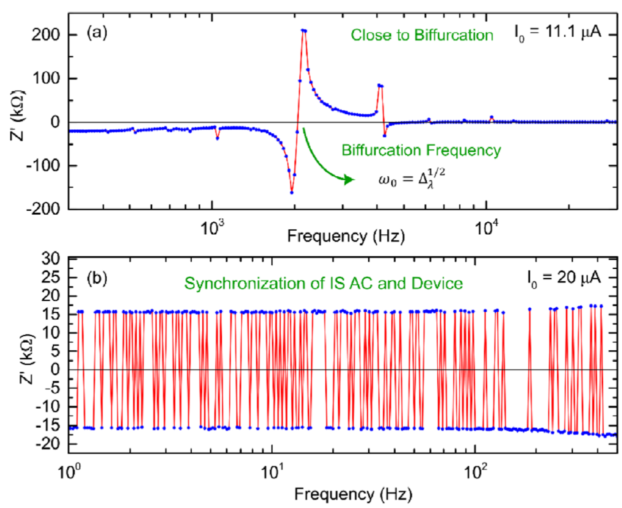

FIGURE 13 | Real-part impedance spectra Z′(f) at I_0 = 11.1 μA (a) and 20 μA (b), plotted in selected zones of the frequency. The blue points represent the fitted experimental data, while the lines are only guides to the eye.

real impedance exhibits a discrete switching between two values of equal magnitude and opposite sign. Remarkably, these values coincide with the magnitude of the impedance reached at these low frequencies. This phenomenon occurs in both oscillatory and non-oscillatory cases; the only requirement is that the low-frequency corner of the spectrum corresponds to a negative real impedance when $Z'' = 0$.

Figure 13 displays the real part of the impedance as a function of frequency for two representative operating points of the system with the oscillation-enabling capacitance, plotted in selected zones of the frequency. Figure 13a corresponds to the orange spectrum in Figure 7, measured in the stable regime, close to the Hopf bifurcation. Figure 13b corresponds to the cyan spectrum in Figure 7, measured within the unstable regime.

Figure 13a provides direct experimental confirmation of the theoretical behavior predicted in Figure 4. The spectrum corresponds to a stable operating point very close to the Hopf bifurcation, where Z' exhibits a clear divergence. This divergence occurs at a frequency of approximately 2 kHz, which should coincide with the oscillation frequency ω_0 at the bifurcation. Using the parameters extracted from the fitted EC and evaluating the bifurcation frequency through Equation (18), we obtain a value that is approximately 2 kHz. The excellent quantitative agreement between the experimentally observed divergence frequency and the theoretically predicted Hopf frequency demonstrates the direct correspondence between the IS response and the underlying bifurcation dynamics, thereby providing experimental validation of the theory illustrated in Figure 4.

Finally, we are going to look into the discrete switching phenomenon introduced previously and visualized in Figure 13b for an operating point within the unstable, self-oscillatory regime. To rationalize this discrete switching of Z' between positive and negative values, it is necessary to revisit the basic principles of IS and the theory of injection locking and entrainment of nonlinear systems. In IS, the condition $Z' < 0$ with $Z'' = 0$ corresponds to a purely NDR. In terms of the raw AC input and output signals used in IS measurements, this implies a phase shift of $\phi = \pi$ between the applied current perturbation and the measured voltage response (whereas a positive resistance corresponds to a phase shift of $\phi = 0$).

The discrete switching observed in Figure 13b reflects transitions between two phase-locked states of the driven response, where the phase difference alternates between $\phi = 0$ and $\phi = \pi$, leading to positive and negative values of Z' with similar magnitude. Importantly, this phenomenon is not exclusive to the oscillatory regime but can also occur in the non-oscillatory case (Figures 6 and 7), indicating that its origin lies in the resonant nature of the equivalent RLC-type circuit rather than in the mere presence of self-sustained oscillations.

Consistent with the periodically forced nonlinear-oscillator theoretical framework introduced above, the observed behavior can be interpreted within the general theory of injection locking and synchronization in nonlinear resonant systems. These theories describe how a driven oscillator can lock its phase to an external sinusoidal perturbation within specific frequency intervals, leading to stable phase configurations of the response. In this context, the discrete switching of the real part of the impedance reflects the existence of multiple phase-locked states of the driven resonant system. A detailed treatment of synchronization theory is beyond the scope of the present work, but the relevant frameworks have been extensively developed in the literature [46, 47].

We therefore conclude that, whenever IS of an equivalent resonant circuit exhibits a purely negative Z' at low frequencies, phase locking between the intrinsic resonant response of the circuit and the externally imposed AC perturbation can occur over finite frequency intervals, giving rise to discrete switching between two phase states and, consequently, between positive and negative values of Z'. This interpretation provides a consistent dynamical explanation for the observed low-frequency sign switching of the real part of the impedance.

7 | Conclusions

This work began by establishing a theoretical framework for S-type NDR oscillators, identifying stable, unstable, and bifurcating regimes and linking each regime directly to its expected IS response. This connection enables the classification of oscillator types and stability domains solely from IS measurements. We then applied this general framework to a specific thyristor model, showing that the theoretical extraction of IS follows the same principles as for a generic S-type oscillator. This consistency allowed for a direct and systematic comparison between theory and experiment.

IS of the thyristor was measured in both non-oscillatory (in the absence of an external oscillation-enabling capacitance) and self-oscillatory conditions (with an added capacitance inducing instability). In both regimes, the experimental spectra were accurately described by the EC representations derived from the theoretical analysis. Moreover, the extracted EC parameters exhibited the same current dependence predicted by the model. A detailed physical interpretation of all observed spectral features was provided, reconciling experimental observations with theoretical predictions and elucidating the dynamical mechanisms underlying the measured responses.

Overall, these results demonstrate the strong potential of IS (a frequency-domain technique traditionally associated with linear systems) to probe intrinsically nonlinear and unstable dynamics such as self-sustained oscillations. Although IS may initially seem ill-suited for systems exhibiting autonomous oscillations, our findings show that it offers a rich and sensitive window into their behavior. IS enables direct experimental identification of stability regimes and bifurcation points without relying on phase-space reconstruction or time-domain nonlinear analysis. The measurements also reveal clear signatures of the interplay between intrinsic oscillations and externally applied small-signal perturbations, including experimental evidence of entrainment and phase locking in resonant NDR systems.

More broadly, this study establishes IS as a powerful in situ probe of nonlinear dynamical phenomena in active electronic and electrochemical devices. By providing direct access to stability, bifurcations, and synchronization effects through frequency-domain measurements, the approach offers a practical bridge between nonlinear dynamics theory, control theory, and experimental device characterization.

8 | Methods

8.1 | Thyristor NDR Device

The anode and gate of the thyristor device (Littelfuse SCR EC103D) were connected with a 150kΩ resistor; this resistance value gives a sufficiently low threshold voltage of approximately 0.8V. Subsequently, the anode and cathode were taken as the 2 terminals.

8.2 | *I–V* and Galvanostatic Impedance Measurements

Electrical measurements were carried out under ambient conditions using a Biologic SP-200 potentiostat. In the current sweep measurement, 1μA/s sweeping rate (1 to 100μA) was used, and the voltage across the working and counter electrode was measured. The NDR region lies between 10 to 60μA. In the impedance measurement, DC currents were varied from 2μA to 80μA. An AC perturbation of 0.2μA peak-to-peak and frequency sweep from 1MHz to 1Hz was used.

9 | Appendix. Characteristics of Bifurcation and Oscillations

To analyze the bifurcation properties that establish the range of oscillatory domains, we consider a linear stability analysis [5, 48]. We expand the Equations (2) and (3) around a stationary point $(\bar{u}, \bar{x})$. The dynamical vector for the small displacement variables $X = [\hat{u}, \hat{x}]$ obeys the differential equation:

$$\frac{dX}{dt} = J\,X \tag{37}$$

Here the Jacobian matrix J is defined by the partial derivatives $F_u = \partial F/\partial u, \ldots$

$$J = \begin{bmatrix} F_u & F_x \\ G_u & G_x \end{bmatrix} \tag{38}$$

We obtain the expressions of the trace

$$T_\lambda = F_u + G_x \tag{39}$$

and the determinant

$$\Delta_\lambda = F_u G_x - F_x G_u \tag{40}$$

The eigenvalues λ of the motion are determined by

$$(J - \lambda\,[1])X = 0 \tag{41}$$

where [1] is the identity matrix. We obtain the characteristic equation

$$\lambda^2 - T_\lambda \lambda + \Delta_\lambda = 0 \tag{42}$$

Hopf bifurcation occurs when a pair of eigenvalues become purely imaginary, i.e., the real part of the eigenvalue changes sign from negative to positive by the variation of a parameter [49, 50], while the determinant is positive.

Acknowledgments

This work was funded by the European Research Council (ERC) via Horizon Europe Advanced Grant, grant agreement n° 101097688 ("PeroSpiker"). Additional institutional support by the Spanish Ministry of Science and Innovation (CEX2021-001230-S grant funded by MCIN/AEI/10.13039/501100011033) is gratefully acknowledged. S.E.N and N.M thank the support from the National Research Foundation (NRF), Singapore, under its Competitive Research Program (CRP) (NRF-CRP25-2020-0002).

Conflicts of Interest

The authors declare no conflicts of interest.

Data Availability Statement

The data presented here can be accessed at https://doi.org/10.5281/zenodo.18801023 (Zenodo) under the license CC-BY-4.0 (Creative Commons Attribution 4.0 International).

References

1. D. V. Christensen, R. Dittmann, B. Linares-Barranco, A. Sebastian, and M. Le Gallo, "2022 Roadmap on Neuromorphic Computing and Engineering," *Neuromorphic Computing and Engineering* 2 (2022): 022501.

2. J. J. Yang, D. B. Strukov, and D. R. Stewart, "Memristive Devices for Computing," *Nature Nanotechnology* 8 (2013): 13–24.

3. Y. Zhang, Z. Wang, J. Zhu, et al., "Brain-Inspired Computing With Memristors: Challenges in Devices, Circuits, and Systems," *Applied Physics Reviews* 7 (2020): 011308.

4. J. Zhu, T. Zhang, Y. Yang, and R. Huang, "A Comprehensive Review on Emerging Artificial Neuromorphic Devices," *Applied Physics Reviews* 7 (2020): 011312.

5. J. Bisquert, R. Fenollosa, A. Cordero, and J. R. Torregrosa, "Bifurcation and Frequency Properties of S-Type Neuronic Oscillators," *The Journal of Physical Chemistry Letters* 16 (2025): 3616–3631.

6. G. Csaba and W. Porod, "Coupled Oscillators for Computing: A Review and Perspective," *Applied Physics Reviews* 7 (2020): 011302.

7. B. Al Beattie, M. Noll, H. Kohlstedt, and K. Ochs, "Oscillator-Based Optimization: Design, Emulation, and Implementation," *The European Physical Journal B* 97 (2024): 7.

8. A. Todri-Sanial, C. Delacour, M. Abernot, and F. Sabo, "Computing With Oscillators From Theoretical Underpinnings to Applications and Demonstrators," *npj Unconventional Computing* 1 (2024): 14.

9. P. Maffezzoni, L. Daniel, N. Shukla, S. Datta, and A. Raychowdhury, "Modeling and Simulation of Vanadium Dioxide Relaxation Oscillators," *IEEE Transactions on Circuits and Systems I: Regular Papers* 62 (2015): 2207–2215.

10. M. Orlik, *Self-Organization in Electrochemical Systems I* (Springer, 2012).

11. A. Wacker and E. Schöll, "Criteria for Stability in Bistable Electrical Devices With S- or Z-Shaped Current Voltage Characteristic," *Journal of Applied Physics* 78 (1995): 7352–7357.

12. Y. Liang, G. Wang, G. Chen, Y. Dong, D. Yu, and H. H. C. Iu, "S-Type Locally Active Memristor-Based Periodic and Chaotic Oscillators," *IEEE Transactions on Circuits and Systems I: Regular Papers* 67 (2020): 5139–5152.

13. P. Strasser, M. Eiswirth, and M. T. M. Koper, "Mechanistic Classification of Electrochemical Oscillators — An Operational Experimental Strategy," *Journal of Electroanalytical Chemistry* 478 (1999): 50–66.

14. J. Bisquert, "Hopf Bifurcations in Electrochemical, Neuronal, and Semiconductor Systems Analysis by Impedance Spectroscopy," *Applied Physics Reviews* 9 (2022): 011318.

15. A. Todri-Sanial, S. Carapezzi, C. Delacour, et al., "How Frequency Injection Locking Can Train Oscillatory Neural Networks to Compute in Phase," *IEEE Transactions on Neural Networks and Learning Systems* 33 (2021): 1996–2009.

16. O. Maher, R. Bernini, N. Harnack, et al., "Highly Reproducible and CMOS-Compatible VO_2-Based Oscillators for Brain-Inspired Computing," *Scientific Reports* 14 (2024): 11600.

17. M. T. M. Koper, "Oscillations and Complex Dynamical Bifurcations in Electrochemical Systems," *Advances in Chemical Physics* 92 (1996): 161–298.

18. K. Krischer, "Nonlinear Dynamics in Electrochemical Systems," in *Advances in Electrochemical Science and Engineering*, ed. R. C. Alkire and D. M. Kolb (Wiley, 2002), 89–208.

19. T. Lan, Q. Qiao, F. Hu, D. Li, and Y. Chen, "Electrochemical Oscillation during the Galvanostatic Charging of $Li_4Ti_5O_{12}$ in Li-Ion Batteries," *The Journal of Physical Chemistry C* 125 (2021): 14549–14558.

20. H. Okada, R. Mizuochi, Y. Sakurada, S. Nakanishi, and Y. Mukouyama, "Electrochemical Oscillations (Named Oscillations H and K) during H_2O_2 Reduction on Pt Electrodes Induced by a Local pH Increase at the Electrode Surface," *Journal of The Electrochemical Society* 168 (2021): 076512.

21. H. Degn, "Theory of Electrochemical Oscillations," *Transactions of the Faraday Society* 64 (1968): 1348–1358.

22. S. Carapezzi, A. Plews, G. Boschetto, A. Nejim, S. Karg, and A. Todri-Sanial, "How Fast Can Vanadium Dioxide Neuron-Mimicking Devices Oscillate? Physical Mechanisms Limiting the Frequency of Vanadium Dioxide Oscillators," *Neuromorphic Computing and Engineering* 3 (2023): 034010.

23. I. Z. Kiss, L. N. Pelster, M. Wickramasinghe, and G. S. Yablonsky, "Frequency of Negative Differential Resistance Electrochemical Oscillators: Theory and Experiments," *Physical Chemistry Chemical Physics* 11 (2009): 5720–5728.

24. S. E. Ng, N. Mathews, R. Fenollosa, J. Rubio-Magnieto, and J. Bisquert, "Capacitive Tuning of Thyristor Oscillators Enables Neuron-Like Signal Amplification," *Physical Review Applied* 25 (2026): 024010.

25. A. Lasia, *Electrochemical Impedance Spectroscopy and its Applications* (Springer, 2014).

26. A. Guerrero, J. Bisquert, and G. Garcia-Belmonte, "Impedance Spectroscopy of Metal Halide Perovskite Solar Cells From the Perspective of Equivalent Circuits," *Chemical Reviews* 121 (2021): 14430–14484.

27. M. E. Orazem and B. Tribollet, *Electrochemical Impedance Spectroscopy*, 2nd ed (Wiley, 2017).

28. T. M. Koper, "Non-Linear Phenomena in Electrochemical Systems," *Journal of the Chemical Society, Faraday Transactions* 94 (1998): 1369–1378.

29. J. Bisquert, "Device Physics Recipe to Make Spiking Neurons," *Chemical Physics Reviews* 4 (2023): 031313.

30. J. Bisquert, "Negative Inductor Effects in Nonlinear Two-Dimensional Systems: Oscillatory Neurons and Memristors," *Chemical Physics Reviews* 3 (2022): 041305.

31. Y. Mukouyama, S. Nakanishi, T. Chiba, K. Murakoshi, and Y. Nakato, "Mechanisms of Two Electrochemical Oscillations of Different Types, Observed for H_2O_2 Reduction on a Pt Electrode in the Presence of a Small Amount of Halide Ions," *The Journal of Physical Chemistry B* 105 (2001): 7246–7253.

32. H. Martínez-García, A. Grau-Saldes, Y. Bolea-Monte, and J. Gámiz-Caro, "On "Discussion on Barkhausen and Nyquist Stability Criteria"," *Analog Integrated Circuits and Signal Processing* 70 (2012): 443–449.

33. S. Hernández and A. Suárez, "Systematic Methodology for the Global Stability Analysis of Nonlinear Circuits," *IEEE Transactions on Microwave Theory and Techniques* 67 (2019): 3–15.

34. L. M. Chua, "Memristor, Hodgkin–Huxley, and Edge of Chaos," *Nanotechnology* 24 (2013): 383001.

35. A. Ascoli, A. S. Demirkol, R. Tetzlaff, S. Slesazeck, T. Mikolajick, and L. O. Chua, "On Local Activity and Edge of Chaos in a NaMLab Memristor," *Frontiers in Neuroscience* 15 (2021): 651452.

36. L. Chua, V. Sbitnev, and H. Kim, "Neurons are Poised Near the Edge of Chaos," *International Journal of Bifurcation and Chaos* 22 (2012): 1250098.

37. D. Ventrice, P. Fantini, D. Betto, G. Carnevale, and A. Benvenuti, "Analytical Model of Deeply-Scaled Thyristors for Memory Applications," in *2012 IEEE Workshop on Microelectronics and Electron Devices* (IEEE, 2012).

38. A. Ascoli, S. Slesazeck, H. Mähne, R. Tetzlaff, and T. Mikolajick, "Nonlinear Dynamics of a Locally-Active Memristor," *IEEE Transactions on Circuits and Systems I: Regular Papers* 62 (2015): 1165–1174.

39. Y. Liang, Q. Zhu, G. Wang, et al., "Universal Dynamics Analysis of Locally-Active Memristors and its Applications," *IEEE Transactions on Circuits and Systems I: Regular Papers* 69 (2022): 1278–1290.

40. J. Grasman, M. J. W. Jansen, and E. J. M. Veling, "Asymptotic Methods for Relaxation Oscillations," in *North-Holland Mathematics Studies*, ed. W. Eckhaus and E. M. de Jager (North-Holland, 1978), 93–111.

41. T. Voglhuber-Brunnmaier and B. Jakoby, "Understanding Relaxation Oscillator Circuits Using Fast-Slow System Representations," *IEEE Access* 11 (2023): 99452–99469.

42. J. Grasman, "Relaxation Oscillations," in *Mathematics of Complexity and Dynamical Systems*, ed. R. A. Meyers, (Springer, 2011), 1475–1488.

43. Y. A. Kuznetsov, *Elements of Applied Bifurcation Theory*, 2nd ed (Springer, 1998).

44. J. Guckenheimer and P. Holmes, *Nonlinear Oscillations, Dynamical Systems, and Bifurcations of Vector Fields* (Springer, 1983).

45. J. Bisquert and A. C. I. Guerrero, "Chemical Inductor," *Journal of the American Chemical Society* 144 (2022): 5996–6009.

46. B. Hong and A. Hajimiri, "A Phasor-Based Analysis of Sinusoidal Injection Locking in LC and Ring Oscillators," *IEEE Transactions on Circuits and Systems I: Regular Papers* 66 (2019): 355–368.

47. F. L. Traversa, M. Di Ventra, F. Cappelluti, and F. Bonani, "Application of Floquet Theory to Dynamical Systems With Memory," *Chaos: An Interdisciplinary Journal of Nonlinear Science* 30 (2020): 123102.

48. M. W. Hirsch, S. Smale, and R. L. Devaney, *Differential Equations, Dynamical Systems, and an Introduction to Chaos*, 3rd ed (Academic Press, 2012).

49. C. P. Fall, E. S. Marland, J. M. Wagner, and J. J. Tyson, *Computational Cell Biology*, (Springer, 2002).

50. C. Koch and I. Segev, *Methods in Neuronal Modeling, Second Edition: From Ions to Networks* (MIT Press, 2003).

Supporting Information

Additional supporting information can be found online in the Supporting Information section.

Supporting File: apxr70141-sup-0001-SuppMat.docx.